Volume 5, Issue VII, July, 2026; No. 90, pp. 1148-1164
Submitted 22/5/2026; Final peer review 30/6/2026
Online Publication 22/7/2026
Available Online at http://www.ijortacs.com

FINITE ELEMENT BASED APPROACH TO MATHEMATICAL MODELING OF FLEXIBLE 3DOF ROBOT ARM

[1]Nwafor Anthony Chigozie, [2]Udeh Chukwuma Callistus
[1]Department of Computer Science; Chukwuemeka Odumegwu Ojukwu University, Uli, Anambra State, Nigeria
[2]Department of computer science, Faculty of Applied and Natural Science, Enugu State, University of Science and Technology (ESUT) Agbani, Nigeria
Email: [1]ac.nwafor@coou.edu.ng, [2]chukwuma.udeh@esut.edu.ng

ABSTRACT

This study presents a finite element-based approach to the mathematical modeling and dynamic analysis of a flexible three-degree-of-freedom (3DoF) robot arm under varying boundary conditions. The motivation for this research stems from the increasing demand for lightweight and flexible robotic manipulators in modern engineering applications, where traditional rigid-body assumptions fail to accurately capture structural behavior. Using the Finite Element Method, the flexible links of the robot arm were discritize and modeled to account for distributed mass, stiffness, and damping properties. Two fundamental boundary condition spinned-free and clamped-free were considered to evaluate their influence on system dynamics. Numerical simulations were conducted in a Python-based environment, where the system's time-domain and frequency-domain responses were analyzed through displacement, velocity, acceleration, phase trajectory, and frequency spectrum plots. The results reveal that the pinned-free configuration exhibits larger displacement amplitudes, lower natural frequencies, and prolonged oscillations due to reduced stiffness at the base. In contrast, the clamped-free configuration demonstrates enhanced stiffness, higher natural frequencies, and faster decay of oscillations, leading to improved stability and control performance. The comparative analysis highlights the critical role of boundary conditions in determining the dynamic behavior of flexible robotic systems. The findings of this study provide valuable insights for the design, modeling, and control of flexible manipulators, particularly in applications requiring high precision and vibration suppression. Ultimately, the research contributes to advancing the development of efficient and reliable flexible robotic systems using robust mathematical modeling techniques.

Keywords: Flexible Robot Arm, 3DoF Manipulator, Finite Element Method, Dynamic Modeling, Boundary Conditions, Vibration Analysis

1. INTRODUCTION

The rapid advancement of automation and intelligent systems has significantly increased the demand for flexible robotic manipulators capable of operating with high precision in dynamic and uncertain environments. Unlike rigid robotic arms, Gungor et al. (2024) revealed that flexible robot arms offer advantages such as reduced weight, lower energy consumption, and improved maneuverability. However, Abdelmaksoud et al. (2024) argued that these benefits come at the cost of increased structural vibrations and complex dynamic behavior, which make accurate modeling and control more challenging. In applications such as space exploration, medical robotics, and lightweight industrial automation, flexible manipulators particularly those with three degrees of freedom (3DoF)are increasingly preferred due to their adaptability and efficiency (Ye et al., 2020; Al Saaideh et al., 2024).

Mathematical modeling plays a critical role in understanding and predicting the behavior of such systems. Traditional modeling techniques (Xu et al., 2021; Pan et al., 2025; Mukhtar et al., 2021), often based on lumped parameter methods or rigid-body assumptions, fail to adequately capture the distributed flexibility and deformation characteristics inherent in flexible robotic arms (Mousa et al., 2024). This limitation has motivated the adoption of more advanced modeling techniques rooted in Finite Element Method (FEM), which provides a systematic framework for discretizing complex structures into smaller elements for precise analysis (Barhaghtalab et al., 2023). FEM enables the incorporation of material properties, geometric nonlinearities, and boundary conditions, making it highly suitable for modeling flexible structures with high fidelity (Hazem et al., 2024).

For a 3DoF flexible robot arm, the interaction between multiple joints and flexible links introduces coupled dynamic effects that are difficult to analyze using simplified analytical methods. The Finite Element Method allows the derivation of accurate system equations by transforming continuous structures into a set of discrete elements governed by differential equations. This facilitates the evaluation of important dynamic characteristics such as natural frequencies, mode shapes, and vibration responses under different loading conditions (Habor et a., 2021). Consequently, FEM-based models provide a strong foundation for designing robust control strategies that can mitigate unwanted oscillations and enhance positioning accuracy (Ashagrie et aal., 2021).Furthermore, Krakhmaev et al. (2021) opined that the integration of FEM with modern computational tools has enabled the simulation of complex robotic systems in real-time or near real-time environments. This is particularly important for validating control algorithms and optimizing system performance before physical implementation (Sahu et al., 2022; Sochima et al., 2025). In the context of flexible 3DoF robot arms, such modeling approaches support the development of advanced controllers, including adaptive, intelligent, and nonlinear control techniques, which are essential for achieving stability and precision in practical applications. Therefore, this study is motivated by the need to develop a comprehensive and accurate mathematical model of a flexible 3DoF robot arm using a finite element-based approach. By addressing the limitations of conventional modeling techniques, the research aims to provide deeper insights into the dynamic behavior of flexible manipulators and contribute to the advancement of efficient, reliable, and high-performance robotic systems.

2. Dynamic Modeling

The flexible body dynamics of the system refer to the deflection of the beam from the expected rigid body position. The equations for this motion can be determined using the Lagrange equations and the assumed modes method (Xu et al., 2023). If the deflection is assumed to be the sum of the generalized coordinates multiplied by shape functions, the equations can be determined by computing the generalized mass, generalized stiffness, generalized force, and generalized moment. The generalized coordinates and shape functions can be determined using the finite-element method as presented in this paper. This is less labor intensive than solving the Euler-Bernoulli beam equation, which is a fourth order partial differential equation (Chavez et al., 2023). Also, system constants such as hub inertia and payload mass must be included in the boundary conditions when solving the partial differential equation. Thus for any changes in these values the equations must be re-solved before a model can be obtained. In the finite-element method this is not necessary and in the resulting total system such values can be updated directly if they change. This is advantageous when modeling a system with varying payload, especially if the model will be used for real-time control.

2.1. Pinned Free Model

Figure 1 shows single link flexible with pinned free boundary conditions. For simplicity, the beam is modeled as a single finite element. This is adequate since the system behavior is dominated by the first mode, which is a relative simple shape function (Azeez et al., 2024). If a pinned-beam is modeled as a single finite element, there are three generalized (independent) coordinates: slope of the beam at the hub, θ_1 the tip deflection, v_2 and the tip slope θ_2. The deflection of the beam at any point along its length is then:

$$y(x,t)=\theta_1(t)\phi_1(x)+v_2(t)\phi_2(x)+\theta_2(t)\phi_3(x) \tag{1}$$

Where ϕ_1 , ϕ_2 and ϕ_3 are the shape functions and x is the distance along the beam. θ_1, v_2 and θ_2 are coordinates of time only, and ϕ_1, ϕ_2 and ϕ_3 are functions of space only (distance, x).

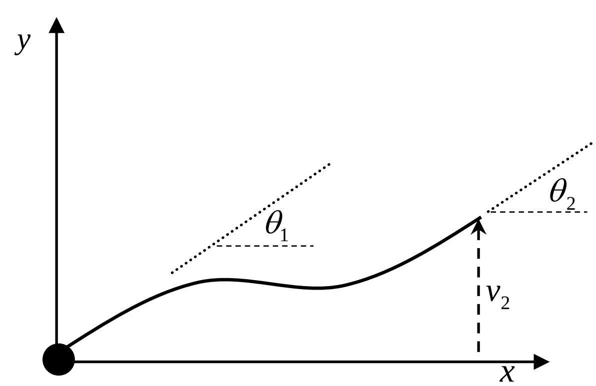

Figure 1 pinned free beam deflections in the x-y

The generalized mass, $\mathbf{M}_B$ and generalized stiffness, $\mathbf{K}_B$ are determined from these shape functions (Barhaghtalab et al., 2023). Knowing these values as well as the generalized forces, M_1, M_2 and F_2, the equation for the flexible body system is:

$$\mathbf{M}_B \begin{bmatrix} \ddot{\theta}_1 \\ \ddot{v}_2 \\ \ddot{\theta}_2 \end{bmatrix} + \mathbf{K}_B \begin{bmatrix} \theta_1 \\ v_2 \\ \theta_2 \end{bmatrix} = \begin{bmatrix} M_1 \\ F_2 \\ M_2 \end{bmatrix} \tag{2}$$

The shape functions must be chosen to satisfy the boundary conditions of the system. For the case of a pinned-free arm the boundary conditions are:

$$\begin{aligned} y(0,t) &= 0 \qquad y(L,t) = v_2 \\ y'(0,t) &= 0 \qquad y'(L,t) = \theta_2 \end{aligned} \tag{3}$$

The beam deflection at any time is chosen to be a third-order polynomial in since this is the lowest order polynomial that can be a solution to the fourth order homogeneous Euler-Bernoulli beam equation. If the beam deflection is chosen as:

$$y(x,t) = a_0 + a_1 x + a_2 x^2 + a_3 x^3 \tag{4}$$

Then based on the boundary conditions, the constants are found to be:

$$\begin{aligned} a_0 &= 0 \\ a_1 &= \theta_1 \\ a_2 &= -\frac{2}{L}\theta_1 + \frac{3}{L^2}v_2 - \frac{\theta_2}{L} \\ a_3 &= \frac{1}{L^2}\theta_1 - \frac{2}{L^3}v_2 + \frac{\theta_2}{L^2} \end{aligned}$$

Substituting these constants into Equation (4) and rearranging gives:

$$y(x,t) = \theta_1(t)\underbrace{\left(x - \frac{2x^2}{L} + \frac{x^3}{L^2}\right)}_{\phi_1} + v_2(t)\underbrace{\left(-\frac{2x^3}{L^3} + \frac{3x^2}{L^2}\right)}_{\phi_2} + \theta_2(t)\underbrace{\left(\frac{x^3}{L^2} - \frac{x^2}{L}\right)}_{\phi_3} \tag{5}$$

$$y(x,t) = \theta_1(t)\phi_1(x) + v_2(t)\phi_2(x) + \theta_2(t)\phi_3(x) \tag{6}$$

The generalized mass matrix is given as (Mukhtar et al., 2021).

$$M_B = \lfloor m_{ij} \rfloor \tag{7}$$

Where $m_{ij} = \int_0^L m(x)\phi_i\phi_j\, dx$; $m(x)$ is the mass per unit length on the beam (assumed to be constant, i.e. $m(x) = m$). The generalized stiffness matrix is given as:

$$K_B = \lfloor k_{ij} \rfloor \tag{8}$$

Where $k_{ij} = \int EI\phi_i\phi_j\, dx$; E is the modulus of elasticity and I is the second moment of area of the arm.For the pinned system, the torque at the hub causes the movement of the arm that leads to a change in θ_1, and the subsequent beam vibration. From the rigid body equations (Brandeen 2001) the torque at hub in terms of motor gear angle is:

$$\tau_{hub} = M_1 = N\left[\tau_a - J_m\ddot{\theta}_m - b_m\dot{\theta}_m\right] - b_s\frac{\dot{\theta}_m}{N} - \left(J_{g2}\right)\frac{\ddot{\theta}_m}{N} \tag{9}$$

$$F_2 = 0$$
$$M_2 = 0$$

Where τ_a, J_m, J_{g2}, b_m: Is the torque supplied by the motor, the moment of inertia of the motor, the moment of inertia of arm gear, the viscous friction of the motor.

The moment M_1 is the equation that links the rigid body to the flexible body. Since the arm angle is related to the motor angle through the gear ratio, the substitution $\theta_1 = \theta_m / N$ is made in Equation (2), and the resulting system has the state variables θ_m, v_2, and θ_2. Therefore, the dynamic equation for the combined rigid-flexible body system is:

$$\mathbf{M}_T\begin{bmatrix}\ddot{\theta}_m\\ \ddot{v}_2\\ \ddot{\theta}_2\end{bmatrix} + \mathbf{B}_T\begin{bmatrix}\dot{\theta}_m\\ \dot{v}_2\\ \dot{\theta}_2\end{bmatrix} + \mathbf{K}_T\begin{bmatrix}\theta_m\\ v_2\\ \theta_2\end{bmatrix} = \mathbf{Q}\tau \tag{10}$$

Where $\mathbf{M}_T = \begin{bmatrix} M_{B11} + NJ_m + \dfrac{\left(J_{g2}\right)}{N} & M_{B12} & M_{B12}\\ M_{B21} & M_{B22} & M_{B23}\\ M_{B31} & M_{B32} & M_{B33}\end{bmatrix}$ $\mathbf{B}_T = \left[\begin{array}{c:c} Nb_m + \dfrac{b_s}{N} & \mathbf{0}_{1\times2}\\ \hdashline \mathbf{0}_{2\times1} & \mathbf{0}_{2\times2}\end{array}\right]$

$$\mathbf{K}_B = \mathbf{K}_T \quad \mathbf{Q} = \begin{bmatrix} 1 \\ 0 \\ 0 \end{bmatrix} \tau = N\tau_a$$

Where b_s the viscous friction of the arm shaft. These equations are written in state-space format as:

$$\begin{aligned} \dot{\mathbf{x}} &= \mathbf{A}\mathbf{x} + \mathbf{B}\mathbf{u} \\ \mathbf{y} &= \mathbf{C}\mathbf{x} \end{aligned} \tag{11}$$

$$\mathbf{x} = \begin{bmatrix} \theta_m \\ v_2 \\ \theta_2 \\ \dot{\theta}_m \\ \dot{v}_2 \\ \dot{\theta}_2 \end{bmatrix}, \quad \mathbf{y} = \begin{bmatrix} \theta_1 \\ v_2 \\ \theta_2 \\ \dot{\theta}_m \\ \dot{v}_2 \\ \dot{\theta}_2 \end{bmatrix}, \ and\ u = \tau = N\tau_a$$

$$\mathbf{A} = \begin{bmatrix} \mathbf{0}_{3\times3} & \mathbf{I} \\ \mathbf{M}_T^{-1}\mathbf{K}_T & \mathbf{M}_T^{-1}\mathbf{B}_T \end{bmatrix}, \ \mathbf{B} = \begin{bmatrix} 0 \\ \mathbf{M}_T^{-1}\mathbf{Q} \end{bmatrix}, \text{ and } \mathbf{C} = \begin{bmatrix} 1/N & \mathbf{0}_{1\times5} \\ \mathbf{0}_{5\times1} & \mathbf{I} \end{bmatrix}$$

A payload mass acts as a force on the end of the beam, F_p where $F_p = m_p\ddot{v}_2$. To include a payload in the calculations, only the mass matrix, $\mathbf{M}_B$ of the flexible body equations changes such that:

$$\mathbf{M}_{B\_payload} = \mathbf{M}_{B\,No\_paylaod} + \begin{bmatrix} 0 & 0 & 0 \\ 0 & m_p & 0 \\ 0 & 0 & 0 \end{bmatrix} \tag{12}$$

2.2 Clamped-Free Beam Model

For the clamped-free beam shown in figure 2 (modeled as a single finite element, there are only two generalized (independent) coordinates: the tip deflection, v_2 and the tip slope θ_2. The deflection of the beam at any point along its length is that:

$$y(x,t) = v_2(t)\phi_1(x) + \theta_2(t)\phi_2(x) \tag{13}$$

Where ϕ_1 and ϕ_2 are the shape functions and x is the distance along the beam. Note that v_2 and θ_2 are functions of time only, ϕ_1 and ϕ_2 are functions of space only.

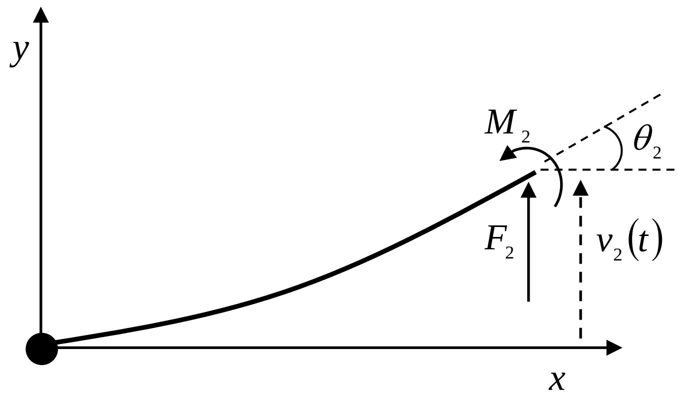

Figure 2 clamped free beam deflection in x-y plane.

The generalized mass, $\mathbf{M}_B$ and generalized stiffness, $\mathbf{K}_B$ are determined from these shape functions. Knowing these values as well as the generalized forces, M_2 and F_2 the equation for the flexible body system is:

$$\mathbf{M}_B\begin{bmatrix}\ddot{v}_2\\ \ddot{\theta}_2\end{bmatrix}+\mathbf{K}_B\begin{bmatrix}v_2\\ \theta_2\end{bmatrix}=\begin{bmatrix}F_2\\ M_2\end{bmatrix} \tag{14}$$

The shape functions must be chosen to satisfy the boundary conditions of the system. For the case of a clamped-free beam the boundary conditions are:

$$\begin{aligned} y(0,t)&=0 \qquad y(L,t)=v_2\\ y'(0,t)&=0 \qquad y'(L,t)=\theta_2 \end{aligned} \tag{15}$$

If, as in Section 2.1, the beam deflection at any time is chosen to be a third-order polynomial in x as in equation (4).Then based on the boundary conditions, the constants evaluate to:

$$a_3=a_4=0$$
$$a_2=\frac{3}{L^2}v_2-\frac{\theta_2}{L}$$
$$a_1=\frac{-2}{L^3}v_2+\frac{\theta_2}{L^2}$$

Substituting these constants and rearranging gives:

$$y(x,t) = v_2(t)\underbrace{\left(-\frac{2x^3}{L^3}+\frac{3x^2}{L^2}\right)}_{\phi_1} + \theta_2(t)\underbrace{\left(\frac{x^3}{L^2}-\frac{x^2}{L}\right)}_{\phi_2} \quad (16)$$

$$y(x,t) = v_2(t)\phi_2(x) + \theta_2(t)\phi_3(x)$$

Depends on the equations (7, & 8) and by using equations (15, 16) can find the generalized mass and stiffness matrix. For the combined system, the loading on the clamped beam is caused by the accelerating hub. The acceleration of the hub, $\ddot{\theta}_a$ causes a distributed force on the beam, $p(x)$ which can be represented by a force and a moment at the tip of the beam, F_2 and M_2 . These can be calculated from the generalized force equations:

$$\begin{aligned} F_2 &= \int_0^L p(x)\phi_1(x)dx \\ M_2 &= \int_0^L p(x)\phi_2(x)dx \end{aligned} \quad (17)$$

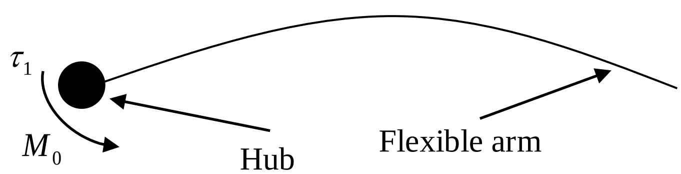

Figure 3:Direction of torque in arm

Where $p(x) = -m\ddot{\theta}_a x$ is the distributed force on the beam:

$$F_2 = \frac{7mL^2}{20}\ddot{\theta}_a = \frac{-7mL^2}{20(N)}\ddot{\theta}_m = F_m\ddot{\theta}_m$$

$$M_2 = \frac{mL^3}{20}\ddot{\theta}_a = \frac{mL^3}{20(N)}\ddot{\theta}_m = M_m\ddot{\theta}_m$$

Figure 3 illustrates the positive direction of the torque acting on the hub (M_o) due to the flexing of the beam when a torque of τ_1, has been applied to the hub. Note that for the deflection shown in Figure 3 the value of M_o will be negative since it opposes the applied torque. The variables τ_1 , ω_m and M_o act on the motor side of the gears. The moment at any point along the arm can be found from $M(x) = EIy''(x,t)$. The equation for the rigid body can now be changed to:

$$\tau_a + M_o = J\ddot{\theta}_m + b\dot{\theta}_m \quad (18)$$

$$M_0 = \frac{M(0)}{N} = \frac{EIy''(0,t)}{N} = \frac{EI}{N}\left(\frac{6}{L^2}v_2 - \frac{2}{L}\theta_2\right)$$

Where M_o is the moment on the hub caused by the flexible body referred to the motor side of the system. The static friction component of T_f must now opposes both τ_a and M_o, when the speed is below the static fiction threshold. Combining the flexible and rigid bodies gives the dynamic equation:

$$\mathbf{M}_T\begin{bmatrix}\ddot{\theta}_m\\ \ddot{v}_2\\ \ddot{\theta}_2\end{bmatrix} + \mathbf{B}_T\begin{bmatrix}\dot{\theta}_m\\ \dot{v}_2\\ \dot{\theta}_2\end{bmatrix} + \mathbf{K}_T\begin{bmatrix}\theta_m\\ v_2\\ \theta_2\end{bmatrix} = \mathbf{Q}\tau \tag{19}$$

Where $\mathbf{K}_T = \left[\begin{array}{cc:c} -\frac{6EI}{NL} & \frac{2EI}{N} & 0 \\ \hdashline \multicolumn{2}{c:}{\mathbf{K}_B} & \begin{matrix}0\\0\end{matrix} \end{array}\right]$, $\mathbf{Q} = \begin{bmatrix}1\\0\\0\end{bmatrix}$, $\mathbf{M}_T = \left[\begin{array}{cc:c} 0 & 0 & J \\ \hdashline \multicolumn{2}{c:}{\mathbf{M}_B} & \begin{matrix}-F_m\\-M_m\end{matrix}\end{array}\right]$, $\mathbf{B}_T = \begin{bmatrix}0 & 0 & b\\0 & 0 & 0\\0 & 0 & 0\end{bmatrix}$

$$\begin{aligned}\dot{\mathbf{x}} &= \mathbf{A}\mathbf{x} + \mathbf{B}\mathbf{u}\\ \mathbf{y} &= \mathbf{C}\mathbf{x}\end{aligned} \tag{20}$$

$$\mathbf{x} = \begin{bmatrix}\theta_m\\ v_2\\ \theta_2\\ \dot{\theta}_m\\ \dot{v}_2\\ \dot{\theta}_2\end{bmatrix}, \quad \mathbf{y} = \begin{bmatrix}\theta_1\\ v_2\\ \theta_2\\ \dot{\theta}_m\\ \dot{v}_2\\ \dot{\theta}_2\end{bmatrix}, \ and\ u = \tau = N\tau_a$$

$$\mathbf{A} = \begin{bmatrix}0 & \mathbf{I}\\ \mathbf{M}_T^{-1}\mathbf{K}_T & \mathbf{M}_T^{-1}\mathbf{B}_T\end{bmatrix},\ \mathbf{B} = \begin{bmatrix}0\\ \mathbf{M}_T^{-1}\mathbf{Q}\end{bmatrix},\ and\ \mathbf{C} = \begin{bmatrix}1/N & \mathbf{0}_{1\times5}\\ \mathbf{0}_{5\times1} & \mathbf{I}\end{bmatrix}$$

Similar to Section 2.1, if a tip mass is included in the calculations, only the mass matrix, $\mathbf{M}_B$ of the flexible body equations changes such that:

$$\mathbf{M}_{B\_payload} = \mathbf{M}_{B\ No\_paylaod} + \begin{bmatrix}m_p & 0\\ 0 & 0\end{bmatrix} \tag{21}$$

3. Simulation experiments

The dynamic simulation of the flexible 3DoF robot arm was carried out using a computational framework derived from the Finite Element Method, where the continuous structure of the manipulator was discretized into equivalent dynamic representations for each degree of freedom. The governing equations of motion were formulated based on second-order differential equations incorporating mass, damping, and stiffness characteristics of the system, with appropriate boundary conditions applied for both pinned-free and clamped-free configurations. A time-domain simulation approach was adopted using numerical integration techniques to evaluate the transient response of the system over a specified duration. The excitation was modeled as an initial disturbance, allowing the natural dynamic behavior of the system to be observed without external forcing. Key state variables, including displacement, velocity, and acceleration, were computed for each joint, while additional analyses such as phase trajectory and frequency-domain transformation using Fast Fourier Transform (FFT) were performed to extract modal characteristics. The simulation environment was implemented in Python, leveraging numerical libraries for efficient computation and visualization, thereby ensuring reproducibility and scalability of the modeling framework. Table 1 and 2 present the simulation parameters.

Table 1: Pinned-Free Conditions

Mode	Amplitude A	Angular Frequency ω (rad/s)	Damping Rate η (s^{-1})
1	0.85	1.4	0.08
2	0.65	1.1	0.10
3	0.55	0.9	0.12

Table 2: Clamped-Free Conditions

Mode	Amplitude A	Angular Frequency ω (rad/s)	Damping Rate η (s^{-1})
1	0.35	3.2	0.22
2	0.28	2.7	0.27
3	0.22	2.2	0.32

4. Results and discussions of the dynamic 3DoF robot arm

The simulation results are presented through a series of graphs that illustrate the dynamic behaviour of the flexible 3DoF robot arm under pinned-free and clamped-free boundary conditions. Each figure provides a specific perspective on the system response, enabling a comprehensive comparison of the two configurations. Figure 4 presents the displacement profiles of all three joints for both boundary conditions. Figure 5 presents velocity response comparison (joint 1)

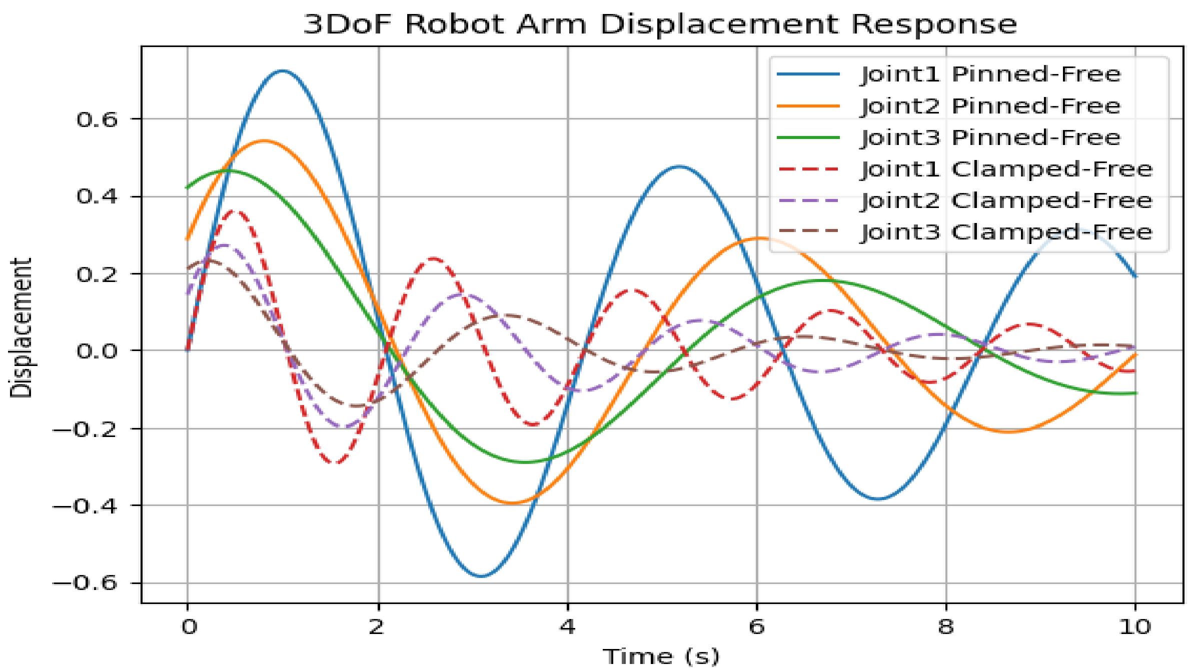

Figure 4: 3DoF Robot Arm Displacement Response.

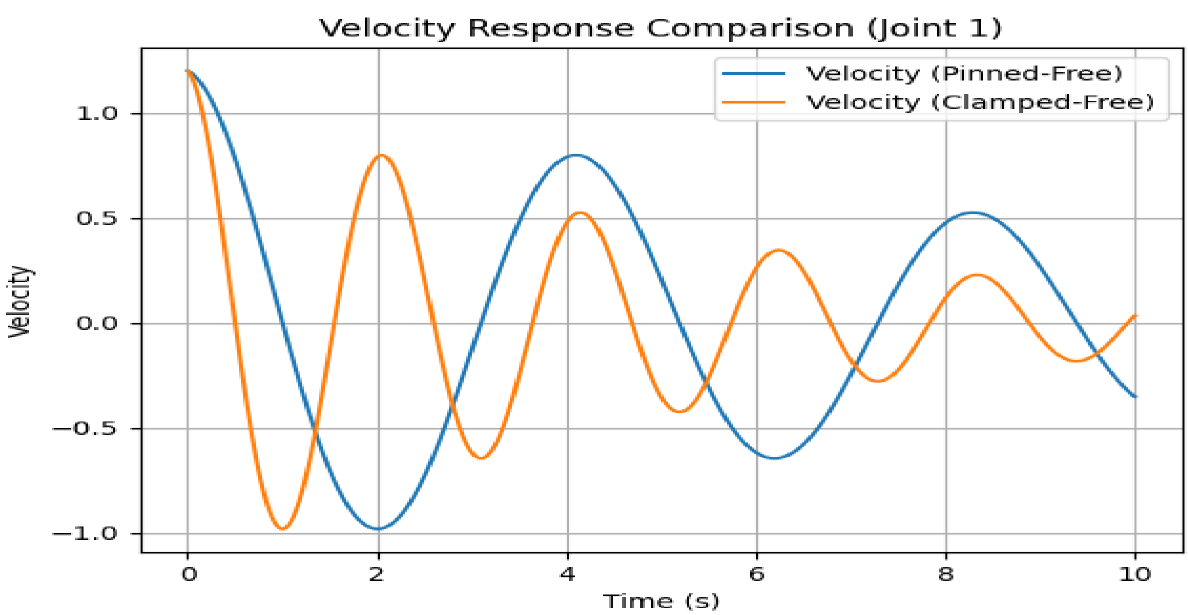

Figure 5: Velocity Response Comparison (Joint 1)

The results in figure 4 clearly show that the pinned-free configuration exhibits significantly higher displacement amplitudes across Joint 1, Joint 2, and Joint 3. The oscillations are more pronounced and persist for a longer duration, indicating lower structural stiffness and reduced damping at the base. Additionally, the phase lag observed between the joints reflects the coupled nature of the system, where motion propagates along the flexible links. In contrast, the clamped-free responses (represented by dashed curves in the figure) display reduced amplitudes and faster decay rates. This behavior confirms that the fixed base condition increases the effective stiffness of the system, thereby limiting excessive deflection and enhancing stability. The rapid attenuation of oscillations in the clamped-free case makes it more suitable for applications requiring high positional accuracy.

Figure 5 illustrates the velocity profiles for the first degree of freedom under both boundary conditions. The clamped-free configuration demonstrates sharper and more frequent velocity peaks, indicating a higher natural frequency and quicker energy exchange within the system. These rapid fluctuations are a direct consequence of the increased stiffness at the base. On the other hand, the pinned-free configuration shows smoother and more gradually varying velocity curves, with lower peak values but sustained oscillations over time. This suggests that although the system experiences less abrupt motion, it remains dynamically active for a longer period. The figure highlights the trade-off between responsiveness and persistence of motion, which is critical in control system design. Figure 6 model the result of acceleration response comparison (joint 1).

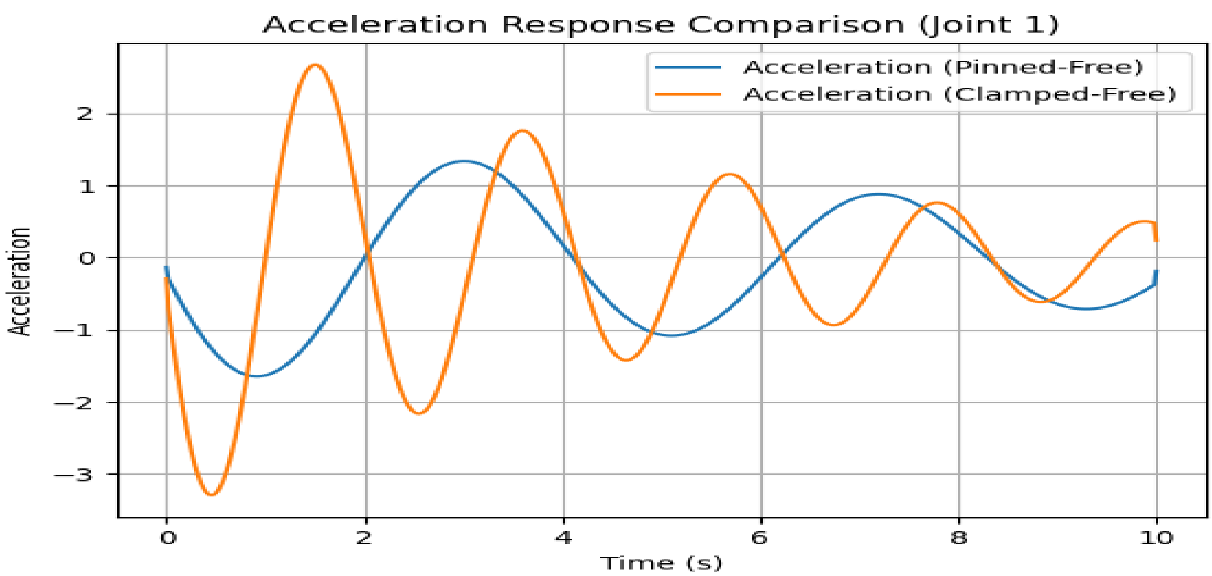

Figure 6: Acceleration Response Comparison (Joint 1)

Figure 6 provides insight into the internal dynamic forces acting within the system. The clamped-free model produces higher initial acceleration peaks, reflecting stronger restoring forces due to the rigid boundary constraint. These peaks diminish rapidly, indicating efficient energy dissipation and quick stabilization. In contrast, the pinned-free configuration exhibits lower acceleration magnitudes but maintains oscillatory behavior over a longer duration. This implies that the forces acting within the system are less intense but more sustained, which may lead to prolonged vibrations and potential structural fatigue. The differences observed in this figure are crucial for evaluating actuator requirements and structural durability. Figure 7 present phase plot (joint 1). Figure 8 is the frequency spectrum (Joint 1) graph.

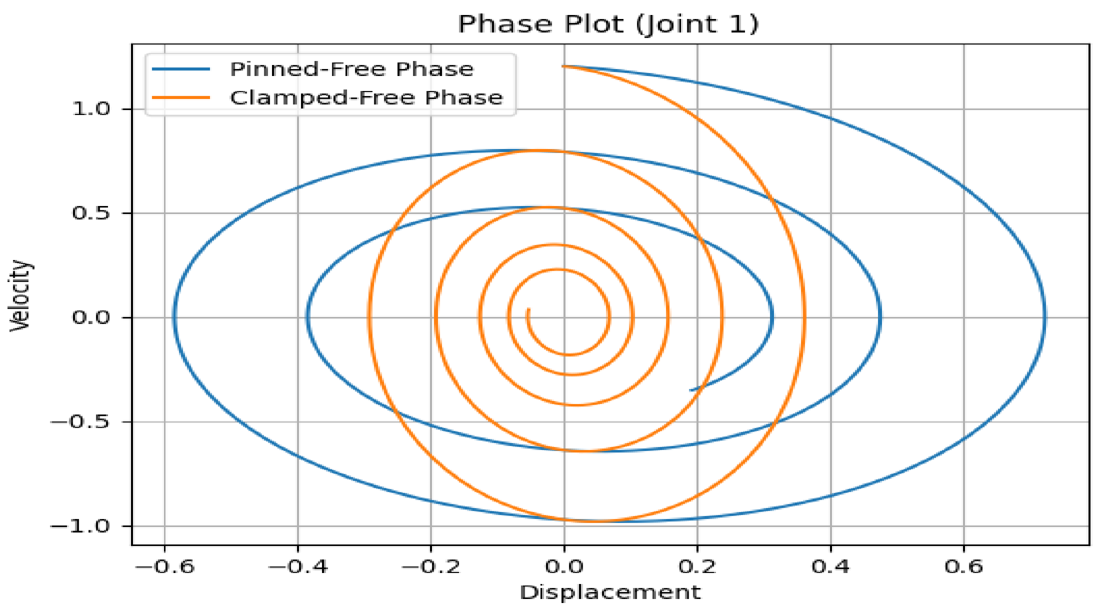

Figure 7: Phase Plot (Joint 1)

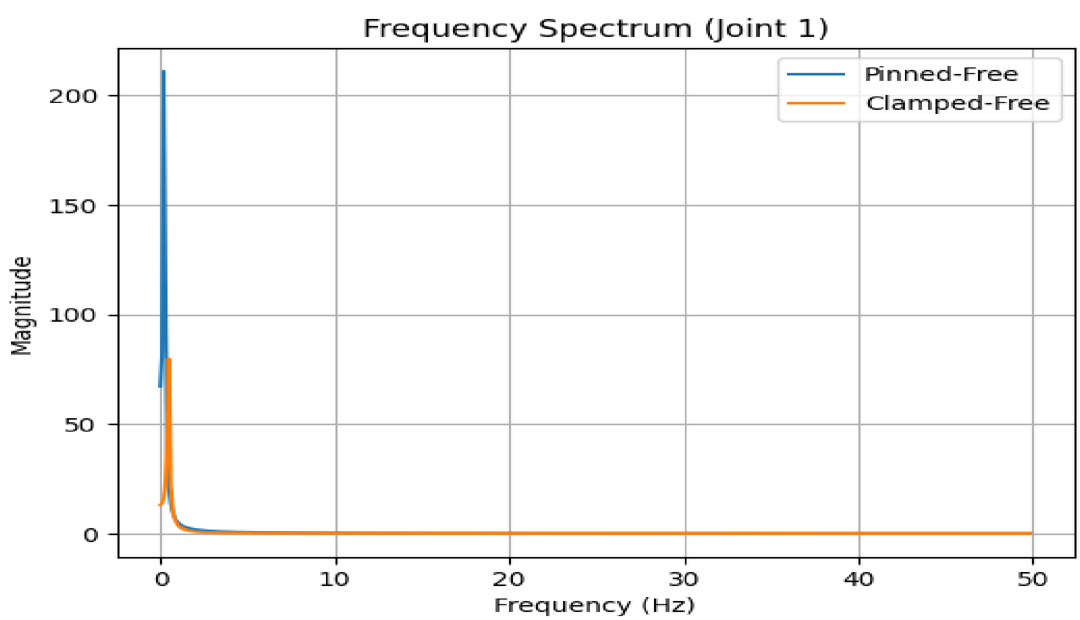

Figure 8: Frequency Spectrum (Joint 1)

Figure 7 shows the relationship between displacement and velocity, offering a graphical representation of system stability and energy dissipation. The pinned-free configuration forms wider and more extended loops, indicating higher energy storage and slower convergence to equilibrium. This reflects the system's tendency to oscillate for longer periods due to lower damping and stiffness. In contrast, the clamped-free configuration produces tighter and more compact phase trajectories, which quickly spiral toward the origin. This behavior signifies rapid stabilization and efficient damping. The figure 7 clearly demonstrates that the clamped-free system possesses superior dynamic stability compared to the pinned-free system.

Figure 8 presents the frequency-domain analysis obtained through Fast Fourier Transform (FFT). The pinned-free configuration shows dominant peaks at lower frequencies, confirming that the system oscillates more slowly due to reduced stiffness. These low-frequency components are associated with larger deformations and higher energy retention. Conversely, the clamped-free configuration exhibits dominant peaks at higher frequencies, indicating a stiffer structure with faster oscillatory behavior. The concentration of energy at higher frequencies suggests a more controlled and predictable response. This figure validates the theoretical expectation that boundary conditions significantly influence the natural frequencies of flexible systems.

Overall, the comparative analysis of the simulation results demonstrates that boundary conditions play a decisive role in shaping the dynamic behavior of flexible robotic manipulators. The pinned-free configuration, while offering greater flexibility, is characterized by larger displacements, prolonged oscillations, and lower natural frequencies, which may compromise precision and stability. On the other hand, the clamped-free configuration provides enhanced stiffness, faster response, and improved damping characteristics, making it more suitable for high-precision applications. However, the increased stiffness also results in higher internal forces, which must be carefully managed in the design process. These findings underscore the importance of accurate modeling and simulation in the development of flexible robotic systems, as they enable informed decisions regarding structural design, control strategies, and operational performance.

5. Conclusion

This study has successfully developed and analyzed a finite element-based mathematical model of a flexible 3DoF robot arm, with particular emphasis on the impact of boundary conditions on system dynamics. By employing the Finite Element Method, the research was able to overcome the limitations of conventional rigid-body modeling approaches and provide a more accurate representation of the distributed flexibility inherent in robotic manipulators. The simulation framework enabled a comprehensive evaluation of the system's dynamic response under pinned-free and clamped-free configurations, capturing key performance indicators such as displacement, velocity, acceleration, phase behavior, and frequency characteristics. The results consistently demonstrate that boundary conditions play a decisive role in shaping the behavior of flexible systems. The pinned-free configuration, characterized by rotational freedom at the base, resulted in larger oscillations, lower stiffness, and slower decay of motion. This makes it less suitable for high-precision applications but useful for understanding worst-case vibration scenarios. On the other hand, the clamped-free configuration provided superior dynamic performance, with reduced displacement amplitudes, higher natural frequencies, and faster stabilization. These characteristics make it more appropriate for practical robotic systems where rigidity and control accuracy are essential. Furthermore, the frequency-domain analysis confirmed that increased stiffness leads to higher dominant frequencies, while the phase-space analysis demonstrated improved energy dissipation in the clamped system. These findings align with theoretical expectations and validate the effectiveness of the modeling approach. Overall, the study establishes a strong foundation for the accurate modeling and analysis of flexible robotic arms and emphasizes the importance of incorporating realistic boundary conditions in simulation and design processes.

5.1 Future Directions

While this study provides a solid framework for modeling and analyzing flexible 3DoF robot arms, several opportunities exist for further research and improvement. First, future work should extend the current model to a full multi-body finite element formulation incorporating nonlinear effects, such as geometric nonlinearity, large deflections, and joint flexibility. This would enhance the realism of the model, especially for applications involving high-speed or large-amplitude motion. Second, the integration of advanced control strategies with the developed model presents a promising direction. Techniques such as adaptive control, robust control, sliding mode control (SMC), and intelligent approaches using artificial intelligence and machine learning can be applied to actively suppress vibrations and improve system performance. This is particularly relevant given the increasing role of smart and autonomous robotic systems in industry.

Another important area for future research is the validation of the simulation results through experimental implementation. Developing a physical prototype of the flexible 3DoF robot arm and comparing experimental data with simulation outcomes would significantly strengthen the credibility and applicability of the model. Additionally, incorporating real-world factors such as sensor noise, actuator limitations, and environmental disturbances would further enhance the robustness of the system. Moreover, future studies can explore the application of this modeling framework to specialized domains such as space robotics, medical robotics, and lightweight industrial manipulators, where flexibility is a critical design consideration. The use of advanced computational tools and real-time simulation platforms can also be investigated to enable hardware-in-the-loop (HIL) testing and digital twin development. In summary, future research should focus on enhancing model complexity, integrating intelligent control systems, validating with experimental data, and expanding application domains. These advancements will contribute to the development of next-generation flexible robotic systems that are efficient, precise, and adaptable to complex operational environments.

6. REFERENCES

Abdelmaksoud SI, Al-Mola MH, Abro GEM, Asirvadam VS. In-depth review of advanced control strategies and cutting-edge trends in robot manipulators: analyzing the latest developments and techniques. IEEE Access. 2024. https://doi.org/10.1109/ACCESS.2024.3383782.

Al Saaideh M, Al-Rawashdeh YM, Aljanaideh K, Zhang L, Boker A, Al Janaideh M. Output feedback control of variable-loaded four-joint manipulators with unknown saturated actuator dynamics. Int J Control Autom Syst. 2024;22(12):3694–707.

Ashagrie A, Salau AO, Weldcherkos T. Modeling and control of a 3-DOF articulated robotic manipulator using self-tuning fuzzy sliding mode controller. Cogent Eng. 2021;8(1):1950105.

Azeez MI, Atia KR. Modeling of PID controlled 3DOF robotic manipulator using Lyapunov function for enhancing trajectory tracking and robustness exploiting Golden Jackal algorithm. ISA Trans. 2024;145:190–204.

Barhaghtalab MH, Sepestanaki MA, Mobayen S, Jalilvand A, Fekih A, Meigoli V. Design of an adaptive fuzzy-neural inference system-based control approach for robotic manipulators. Appl Soft Comput. 2023;149: 110970.

Chávez-Vázquez S, Lavín-Delgado JE, Gómez-Aguilar JF, Razo-Hernández JR, Etemad S, Rezapour S. Trajectory tracking of Stanford robot manipulator by fractional-order sliding mode control. Appl Math Model. 2023;120:436–62.

Gungor G, Afshari M. Sensorimotor control using adaptive neuro-fuzzy inference for human-like arm movement. Appl Sci. 2024;14(7):2974.

Harbor M.C, Eneh I.I., Ebere U.C. (2021). Nonlinear dynamic control of autonomous vehicle under slip using improved back-propagation algorithm. International Journal of Research and Innovation in Applied Science (IJRIAS); Vol. 6; Issue 9; https://rsisinternational.org/journals/ijrias/DigitalLibrary/volume-6-issue-9/62-68.pdf

Hazem ZB, Guler N, El Fezzani W. Study of inverse kinematics solution for a 5-axis mitsubishi rv-2aj robotic arm using deep reinforcement learning. In: Guler N, editor. Business sustainability with Artificial Intelligence (AI): challenges and opportunities, vol. 2. Cham: Springer Nature Switzerland; 2024. p. 381–93.

Krakhmalev O, Krakhmalev N, Gataullin S, Makarenko I, Nikitin P, Serdechnyy D, Liang K, Korchagin S. Mathematics model for 6-DOF joints manipulation robots. Mathematics. 2021;9(21):2828.

Mousa M, Al-Mahasneh A, Baniyounis M, Biesenbach R, Falkenhain J. Development of ANFIS controller for trajectory tracking control using ROBO2L MATLAB toolbox for KUKA industrial Robot via RSI. In: 2024 21st international multi-conference on systems, signals & devices (SSD). IEEE; 2024. p. 110–117.

Mukhtar M, Khudher D, Kalganova T. A control structure for ambidextrous robot arm based on Multiple Adaptive Neuro-Fuzzy Inference System. IET Control Theory Appl. 2021;15(11):1518–32.

Pan J. Fractional-order sliding mode control of manipulator combined with disturbance and state observer. Robot Auton Syst. 2025;183: 104840.

Sahu VSDM, Samal P, Panigrahi CK. Modelling, and control techniques of robotic manipulators: A review. Mater Today Proc. 2022;56:2758–66.

Sochima V.E. Asogwa T.C., Lois O.N. Onuigbo C.M., Frank E.O., Ozor G.O., Ebere U.C. (2025)"; Comparing multi-control algorithms for complex nonlinear system: An embedded programmable logic control applications; DOI: http://doi.org/10.11591/ijpeds.v16.i1.pp212-224

Xu K, Wang Z. The design of a neural network-based adaptive control method for robotic arm trajectory tracking. Neural Comput Appl. 2023;35(12):8785–95.

Xu Y, Liu R, Liu J, Zhang J. A novel constraint tracking control with sliding mode control for industrial robots. Int J Adv Rob Syst. 2021;18(4):17298814211029778.

Ye H, Wang D, Wu J, Yue Y, Zhou Y. Forward and inverse kinematics of a 5-DOF hybrid robot for composite material machining. Robot ComputIntegr Manuf. 2020;65: 101961.